Nitrogen and Carbon fractionation during core–mantle differentiation at shallow depth

Article *in* Earth and Planetary Sciences Letters · December 2016

DOI: 10.1016/j.epsl.2016.10.026

5 authors, including:

Celia Dalou
Centre de Recherches Pétrographiques et Gé…
28 PUBLICATIONS **146** CITATIONS
SEE PROFILE

Marc Hirschmann
University of Minnesota Twin Cities
212 PUBLICATIONS **9,726** CITATIONS
SEE PROFILE

Anette von der Handt
University of Minnesota Twin Cities
61 PUBLICATIONS **447** CITATIONS
SEE PROFILE

Earth and Planetary Science Letters ••• (••••) •••–•••

Contents lists available at ScienceDirect

Earth and Planetary Science Letters

www.elsevier.com/locate/epsl

Nitrogen and carbon fractionation during core–mantle differentiation at shallow depth

Celia Dalou *, Marc M. Hirschmann, Anette von der Handt, Jed Mosenfelder, Lora S. Armstrong

Dept. of Earth Sciences, 108 Pillsbury Hall, University of Minnesota, Minneapolis, MN 55455, USA

ARTICLE INFO

Article history:
Received 21 May 2016
Received in revised form 8 October 2016
Accepted 15 October 2016
Available online xxxx
Editor: B. Marty

Keywords:
nitrogen
carbon
partition coefficients
metal
silicate
core

ABSTRACT

One of the most remarkable observations regarding volatile elements in the solar system is the depletion of N in the bulk silicate Earth (BSE) relative to chondrites, leading to a particularly high and non-chondritic C:N ratio. The N depletion may reflect large-scale differentiation events such as sequestration in Earth's core or massive blow off of Earth's early atmosphere, or alternatively the characteristics of a late-added volatile-rich veneer. As the behavior of N during early planetary differentiation processes is poorly constrained, we determined together the partitioning of N and C between Fe–N–C metal alloy and two different silicate melts (a terrestrial and a martian basalt). Conditions spanned a range of f_{O_2} from ΔIW−0.4 to ΔIW−3.5 at 1.2 to 3 GPa, and 1400 °C or 1600 °C, where ΔIW is the logarithmic difference between experimental f_{O_2} and that imposed by the coexistence of crystalline Fe and wüstite.

N partitioning ($D_N^{metal/silicate}$) depends chiefly on f_{O_2}, decreasing from 24 ± 3 to 0.3 ± 0.1 with decreasing f_{O_2}. $D_N^{metal/silicate}$ also decreases with increasing temperature and pressure at similar f_{O_2}, though the effect is subordinate. In contrast, C partition coefficients ($D_C^{metal/silicate}$) show no evidence of a pressure dependence but diminish with temperature. At 1400 °C, $D_C^{metal/silicate}$ partition coefficients increase linearly with decreasing f_{O_2} from 300 ± 30 to 670 ± 50. At 1600 °C, however, they increase from ΔIW−0.7 to ΔIW−2 (87 ± 3 to 240 ± 50) and decrease from ΔIW−2 to ΔIW−3.3 (99 ± 6). Enhanced C in melts at high temperatures under reduced conditions may reflect stabilization of C–H species (most likely CH_4). No significant compositional dependence for either N or C partitioning is evident, perhaps owing to the comparatively similar basalts investigated.

At modestly reduced conditions (ΔIW−0.4 to −2.2), N is more compatible in core-forming metal than in molten silicate ($1 \leq D_N^{metal/silicate} \leq 24$), while at more reduced conditions (ΔIW−2.2 to ΔIW−3.5), N becomes more compatible in the magma ocean than in the metal phase. In contrast, C is highly siderophile at all conditions investigated ($100 \leq D_C^{metal/silicate} \leq 700$). Therefore, sequestration of volatiles in the core affects C more than N, and lowers the C:N ratio of the BSE. Consequently, the N depletion and the high C:N ratio of the BSE cannot be explained by core formation. Mass balance modeling suggests that core formation combined with atmosphere blow-off also cannot produce a non-metallic Earth with a C:N ratio similar to the BSE, but that the accretion of a C-rich late veneer can account for the observed high BSE C:N ratio.

1. Introduction

The global reservoirs and fluxes of nitrogen and carbon are key considerations for the maintenance of the terrestrial atmosphere, habitability, and biosphere (e.g. Sleep and Zahnle, 2001). In the last decade, the deep carbon cycle and inventories have received considerable attention (cf., Dasgupta, 2013), and in recent years there has been growing focus on nitrogen (e.g., Johnson and Goldblatt, 2015 and the references therein). When examining the origin of global inventories and deep cycling, it is natural to compare nitrogen and carbon together because both are volatile during mantle degassing, incompatible during mantle melting and siderophile during core formation (e.g., Miyazaki et al., 2004; Dasgupta, 2013; Roskosz et al., 2013; Li et al., 2016).

A remarkable feature of BSE N inventory is the apparent depletion relative to C as well as other major volatiles and rare gases, though the magnitude of this depletion is debated (e.g.

* Corresponding author.
E-mail address: celia.dalou@gmail.com (C. Dalou).

http://dx.doi.org/10.1016/j.epsl.2016.10.026
0012-821X/

Marty, 2012; Johnson and Goldblatt, 2015; Hirschmann, 2016). Evidence for the depletion of volatile ratios such as C/N derives from mass balance calculations inventorying the mantle, crust and atmosphere (Marty, 2012; Bergin et al., 2015). Possible explanations for the apparent N depletion include atmospheric escape (Tucker and Mukhopadhyay, 2014; Hirschmann, 2016) or a deep N reservoir not sampled by oceanic basalt generation (Johnson and Goldblatt, 2015). Alternatively, the N depletion of the BSE could have been caused by the segregation of core-forming metal segregated from the magma ocean (Marty, 2012; Roskosz et al., 2013). Iron nitrides are stable at high pressure and temperature (Adler and Williams, 2005) and N solubility in molten alloys is 3–4 orders of magnitude larger than in silicates at low pressure (e.g. Miyazaki et al., 2004), consistent with the hypothesis that the core may be an appreciable N reservoir.

Determining the fraction of terrestrial N that was removed from the BSE by core formation requires constraints on N partitioning between molten Fe-rich alloy and silicate melt ($D_N^{metal/silicate}$). Preliminary estimates based on comparison between low-pressure solubilities of N_2 in alloy and silicate melt suggested extremely strong siderophile behavior, with $D_N^{metal/silicate}$ similar to 10,000 (Miyazaki et al., 2004). If applicable to core formation, such extreme values imply N masses in the core hundreds of times greater than that in the atmosphere (Miyazaki et al., 2004). However, such estimates are likely misleading, as they are predicated on the limited solubility of molecular N_2 in silicate melts, whereas melts in equilibrium with molten Fe would likely dissolve N more readily in a reduced species such as N^{3-} or N–H complexes (Miyazaki et al., 2004; Mysen and Fogel, 2010; Kadik et al., 2015). N partitioning between metal and silicate measured at high pressure is more modest. Coexisting Fe–Ni–N molten alloy and silicate liquid similar in composition to chondritic meteorites (Roskosz et al., 2013) yielded $D_N^{metal/silicate}$ values that range from ~3 to 20, with values increasing modestly with pressure from 1.8 to 17.7 GPa (at 2227 to 2577 °C) over a narrow range of oxygen fugacity, f_{O_2} (ΔIW−2.2 to −1.0, where ΔIW is the logarithmic difference between experimental f_{O_2} and that of the iron–wüstite buffer, and all published values of ΔIW have been adjusted according to the calculator of Wade and Wood (2005), as described in greater detail below). The effect of variable f_{O_2} (ΔIW−0.7 to −3.7) on N partitioning was explored by Kadik et al. (2011, 2015) for Fe-rich alloys and silicic (62–75 wt.% SiO_2) FeO–Na_2O–Al_2O_3–SiO_2 melts at 1.5 GPa and 1400 °C, and comparatively small (0.5–2.9) $D_N^{metal/silicate}$ values were found which show a crude trend to greater $D_N^{metal/silicate}$ at greater f_{O_2}. In comparison, at less reduced conditions (ΔIW−0.8 to 0.5), Li et al. (2016) measured larger $D_N^{metal/silicate}$(8–149) between 1.5 and 7 GPa and 1600–1700 °C, and suggested a linear increase in $\log D_N^{metal/silicate}$ with $\log f_{O_2}$.

It is well established that C is highly siderophile over a large range of pressures, temperatures, and f_{O_2} (Dasgupta et al., 2013 at 1 to 5 GPa, 1600 and 2000 °C and ΔIW−0.5 to −1.8; Chi et al., 2014 at 1 to 3 GPa, 1500 and 1800 °C and ΔIW−0.4 to −1.5; Stanley et al., 2014 at 1 to 3 GPa, 1350 and 1620 °C and ΔIW−0.3 to −0.6; Li et al., 2015 at 3 GPa, 1600 °C and ΔIW−0.6 to −4.7; Armstrong et al., 2015 at 1.2 GPa, 1400 °C and ΔIW−0.1 to −3.0). Accordingly, the core is thought to be a significant sink for terrestrial C (e.g. Wood, 1993; Dasgupta et al., 2009; Wood et al. 2013), and C is considered to be among the light elements likely to contribute to the physical properties of the core, together with S, O, Si and H (e.g. Righter, 2003). However, constraining the influence of core formation on the C:N ratio of the BSE requires data on both N and C partitioning between metal alloy and silicate melts, and to date no study has determined these simultaneously.

In the present work, N and C partition coefficients between metal alloy and silicate melts were measured from the same experiments at conditions relevant to core–mantle differentiation at shallow depth. We present 29 new alloy/glass pairs to compare the effects of f_{O_2}, P, T, and melt composition on both N and C partition coefficients. The experiments were conducted at 1.2 to 3 and 1400 °C or 1600 °C, over a large range of f_{O_2} (ΔIW−0.4 to −3.5), employing either a terrestrial or martian basalt.

2. Methods

2.1. Experimental and analytical techniques

Two starting materials were used. The first is a martian basalt based on the Adirondack-class Humphrey basalts from Gusev Crater, Mars, close in composition to those used by Stanley et al. (2014) and Armstrong et al. (2015). The second is modeled after primary normal MORB (N-MORB) close in composition to that used by Armstrong et al. (2015). Both were prepared initially iron-free by mixing pre-dried spectroscopically pure oxides and carbonates in ethanol in an agate mortar for 1 h. The mixes were decarbonated by slow heating (200 °C/h) up to 900 °C and then held for 2 h and ground again in ethanol in an agate mortar for 1 h. After decarbonation, Fe oxide was added as FeO, as iron in the melt should be nearly entirely ferrous under the reducing conditions anticipated.

Nitrogen was introduced as Fe_4N and/or Si_3N_4 (Table 1). Up to 16 wt.% of Fe_4N was added to yield charges with 1 wt.% N in the starting material. Because of its strong reducing effect (Eq. (1)), Si_3N_4 was used chiefly to control the f_{O_2} of experiments based on the reaction:

$$6\ \underset{\text{silicate melt}}{FeO} + \underset{\text{nitride}}{Si_3N_4} = 6\ \underset{\text{alloy}}{Fe} + 3\ \underset{\text{silicate melt}}{SiO_2} + 2\ \underset{\text{silicate melt or alloy}}{N_2} \quad (1)$$

Samples were loaded into graphite capsules to avoid Fe and N loss to metal containers, ensure reducing conditions, and to provide a source of C. Up to six different compositions were loaded into individual holes drilled in to a single graphite capsule in order to achieve variable f_{O_2} conditions at fixed P and T in the same experiment (Table 1).

Experiments were carried out in a half-inch piston cylinder at 1.2, 2, 2.2, or 3 GPa and 1400 or 1600 °C (Table 1). Assemblies comprise, from inside to outside: MgO cell parts (dried at 1000 °C for 4 h and stored in a drying oven at 110 °C) surrounded by a graphite furnace and either CaF_2 sleeves (experiments at 1400 °C) or $BaCO_3$ sleeves (experiments at 1600 °C). The graphite capsule was placed in an MgO sleeve and isolated from the thermocouple by a 1 mm MgO disc, leading to a 12 °C difference between the top of the sample and the tip of the thermocouple based on previous calibrations (Xirouchakis et al., 2001). The temperature was measured to within ±2 °C of the set point using a type B ($Pt_{70}Rh_{30}$/$Pt_{94}Rh_6$) thermocouple. From pressure-calibration using the reaction grossular + kyanite + quartz = anorthite (Xirouchakis et al., 2001), a pressure correction of 0.2 GPa was applied to the experiments using $BaCO_3$ cells. No friction correction was applied to experiments in the CaF_2 cells. Experimental durations were 6 h for 1400 °C experiments following previous work (Stanley et al., 2014; Armstrong et al., 2015), and 4 h for 1600 °C experiments. Experiments were quenched at rates of ~125 °C/s for $BaCO_3$ and 175 °C/s for CaF_2 cells, respectively (Zhang et al., 2016), by cutting power to the furnace. Recovered capsules were mounted in ethyl-2-cyanoacrylate ("superglue") and polished for electron microprobe analysis (EPMA). Subsequently the samples were removed from the superglue with acetone and prepared for secondary ion mass spectrometry (SIMS) analysis as described below.

Major element and N concentrations of silicate glasses and alloys were analyzed on a JEOL JXA-8900R EPMA at the University

Please cite this article in press as: Dalou, C., et al. Nitrogen and carbon fractionation during core–mantle differentiation at shallow depth. Earth Planet. Sci. Lett. (2016), http://dx.doi.org/10.1016/j.epsl.2016.10.026

Table 1
Experimental conditions, starting compositions, and redox conditions.

	P (GPa)	T (°C)	Composition	Fe_4N (wt.%)	Si_3N_4 (wt.%)	Fe (wt.%)	log f_{O_2} ΔIW
B700	1.2	1400	Humphrey	16	–	–	−0.703
B697				16	0.5	–	−2.014
B693				–	2.5	10	−3.498
B690				–	2.5	5	−3.378
B706a				16	0.5	–	−1.175
B706b				16	2	–	−1.329
B706c				9	–	–	−0.659
B699c	2.2	1400	Humphrey	16	–	–	−0.545
B699a				16	0.5	–	−1.091
B699b				16	1	–	−2.123
B707b				9	–	–	−0.421
B707c				16	2	–	−0.909
B712a	2	1600	Humphrey	9	–	–	−0.701
B712b				–	2.5	–	−3.302
B712c				16	0.5	–	−1.057
B712d				16	2	–	−2.053
B712e				16	1	–	−1.235
B712f				16	–	–	−0.771
B727a	2	1600	MORB	16	–	–	−1.265
B727b				16	0.5	–	−1.101
B727c				16	1	–	−1.417
B727d				16	2	–	−1.838
B727e				–	2.5	–	−1.800
B727f				9	–	–	−1.322
B714a	3	1600	Humphrey	16	–	–	−0.441
B714b				16	0.5	–	−1.075
B714c				16	2	–	−1.641
B714d				16	1	–	−1.132
B714e				–	2.5	–	−2.352

of Minnesota. The analytical procedure includes separate acquisitions for major elements and N in samples and standards. Analytical conditions used for glasses and alloys were 15 kV and 20 nA for major elements and 10 kV and 150 nA for N. Major element and N data were processed together in the ProbeforEPMA software using the PROZA algorithm (Bastin et al., 1998) and FFAST mass absorption coefficients (Chantler et al., 2005), which yield an accuracy within 10% on N standards. Further details of the N analytical procedure are given in Von der Handt and Dalou (2016). Silicate minerals and synthetic oxides were employed as standards for major elements and silicon nitride (Si_3N_4) was used as a standard for N. Exponential background models for N were fitted to wavelength scans on both samples and standards. Count times were 20 s on peak and 20 s off-peak for major elements in glasses and alloys. Nitrogen in glasses and metals was measured for 80 s on peak and 120 s off-peak on two LDE1 crystals and their net intensities were aggregated. These two crystals are located on opposite sides of the sample chamber, allowing us to monitor artifacts related to sample relief (i.e. metal in cracks in the sample surface, or effects from edge rounding). Since light elements like N are analyzed from a very shallow region in the sample, they are very sensitive to surface roughness. Only N data agreeing within analytical errors were considered. This procedure yields detection limits of 0.03 wt.% N in glasses and alloys.

Carbon and hydrogen in glasses were measured by SIMS on the Cameca 6f at Arizona State University. Following previously established protocols (e.g. Aubaud et al., 2007), samples and standards were cleaned, dried, and pressed into a single indium mount that was subsequently gold coated. We used a Cs^+ primary beam running at 8–10 nA with an impact energy of 19 keV, tuned for each analysis in critical illumination mode. Ion imaging was employed where necessary in order to preclude analysis of Fe-rich metal phases. Charge compensation was achieved using a normal incidence electron flood gun. Samples were pre-sputtered for 3 min using a 35 μm square raster, and a 100 μm field aperture was used to collect ions restricted to the central 8 μm of each crater. For each analysis, ^{12}C, $^{16}O^1H$, ^{18}O, and ^{30}Si negative ions were detected using an electron multiplier, with counts corrected for detector background and counting system deadtime. A mass resolving power of ∼5000 ($M/\Delta M$) was used to resolve $^{16}O^1H$ from ^{17}O.

Carbon was determined from $^{12}C/^{18}O$, calibrated using four synthetic CO_2-bearing basaltic glasses (B248, B274, B291 and B311) from Stanley et al. (2014). Hydrogen contents (expressed as H_2O) were calculated from $^{16}O^1H/^{18}O$, calibrated using four natural hydrous basaltic glasses (ALV519-4-1, JdFD10, KN54Sta51 and KN54Sta52; Aubaud et al., 2007). All analyses were blank corrected using periodic measurements of GRR1017, a dry synthetic forsterite (Mosenfelder et al., 2011), and standards were analyzed multiple times during the session. Although we report the concentrations as total H_2O (Table 2), comparison to glasses synthesized under comparable conditions by Armstrong et al. (2015) implies that our glasses contain multiple hydrous species, including combinations of OH, N–H compounds, C–H compounds and H_2, depending on experimental conditions. Thus our reported concentrations may represent contributions from all of these species, depending on dissociation of molecular ions and recombination reactions occurring at or near the sample surface during sputtering. Internal precision for each analysis was 4% or less for $^{12}C/^{18}O$ and 1% for $^{16}O^1H/^{18}O$. Data are presented in Table 2, with errors given as one standard deviation ($1\sigma_{SD}$) of 2–5 analyses per sample.

3. Results

3.1. Sample description

All experimental charges are composed of a graphite-saturated mafic glass coexisting with variable amounts of an iron carbide

Table 2
Volatile element partitioning between metal alloys and silicate melts.

Samples	log f_{O_2} ΔIW	Fe–N–C metal alloy		Silicate melt			D_N	D_C	D_P
		N EPMA (wt.%)	C EPMA (wt.%)[a]	N EPMA (wt.%)	C SIMS (ppm)	Total H_2O[b] SIMS (wt.%)			
B700	−0.70	0.96(4)	3.92(30)	0.040(5)	na	na	24(3)	–	0.52(23)
B697	−2.01	0.98(3)	3.26(10)	0.18(1)	49(3)	0.344(7)	5.5(4)	666(46)	56(32)[*]
B693	−3.50	1.00(50)	2.6(17)	3.89(2)	na	na	0.3(1)	–	–
B690	−3.38	1.04(36)	3.2(20)	3.54(9)	na	na	0.3(1)	–	–
B706a	−1.18	1.05(3)	4.05(30)	0.09(1)	78(1)	0.68(1)	12(2)	519(39)	7.8(10)
B706b	−1.33	1.08(1)	4.22(43)	0.09(1)	70(1)	0.500(4)	12(2)	604(62)	10(10)
B706c	−0.66	0.99(2)	4.15(17)	0.04(1)	110(1)	1.043(5)	23(4)	378(16)	0.27(14)[d]
B699c	−0.55	2.00(5)	3.91(29)	0.09(2)	na	na	21(4)	–	0.38(25)
B699a	−1.09	2.12(15)	3.59(20)	0.26(2)	na	na	8.0(8)	–	17.6(77)
B699b	−2.12	1.93(88)	3.03(57)	0.79(2)	na	na	3(1)	–	48(57)[d]
B707b	−0.42	1.97(7)	4.28(17)	0.13(2)	141(11)	1.29(10)	15(3)	304(26)	0.19(9)
B707c	−0.91	1.82(8)	4.26(33)	0.23(1)	101(19)	0.86(2)	8.1(5)	422(86)	4.74(86)
B712a	−0.70	1.86(13)	4.22(13)	0.14(1)	487(1)	0.716(1)	14(2)	87(3)	0.57(10)
B712b	−3.30	1.54(21)	3.96(22)	4.76(3)	401(7)	0.191(2)	0.32(4)	99(6)	106(42)[d]
B712c	−1.06	1.81(2)	3.86(20)	0.12(2)	na	na	15(2)	–	2.03(36)
B712d	−2.05	1.64(33)	4.64(93)	0.78(1)	195(2)	0.289(4)	2.1(4)	238(48)	71(67)
B712e	−1.24	1.78(3)	4.11(23)	0.26(1)	258(5)	0.49(2)	6.8(2)	159(9)	10(6)
B712f	−0.77	1.93(6)	4.28(15)	0.14(2)	328(71)	0.721(5)	14(2)	130(29)	1.77(27)
B727a	−1.27	2.03(8)	4.28(50)	0.34(2)	212(5)	0.415(3)	5.9(3)	202(24)	17(5)
B727b	−1.10	1.98(6)	3.78(45)	0.21(2)	270(16)	0.75(1)	9.2(9)	140(19)	1.78(71)
B727c	−1.42	1.96(5)	3.84(28)	0.16(3)	192(5)	0.604(3)	12(2)	200(16)	3.5(14)
B727d	−1.84	1.89(8)	4.05(57)	0.19(2)	213(83)	1.02(2)	10(1)	190(79)	
B727e	−1.80	1.96(4)	4.1(16)	0.24(1)	270(13)	0.57(1)	8.2(4)	150(60)	3.6(22)
B727f	−1.32	1.96(3)	3.78(19)	0.26(1)	222(17)	0.33(1)	7.6(3)	170(16)	4.9(16)
B714a	−0.44	3.66(73)	4.01(80)	0.17(2)	na	na	21(4)	–	1.27(45)
B714b	−1.08	3.20(3)	4.42(40)	0.43(1)	239(7)	0.493(2)	7.5(2)	185(17)	7.9(23)
B714c	−1.64	3.49(24)	3.36(37)	1.230(2)	166(9)[c]	0.361(4)[c]	2.8(2)	203(25)	102(100)[d]
B714d	−1.13	3.31(4)	3.21(27)	0.38(2)	223(38)	0.59(2)	8.8(4)	144(27)	7.1(12)
B714e	−2.35	3.54(57)	3.56(53)	5.42(1)	263(32)	0.362(6)	0.7(1)	135(26)	–

Numbers in parentheses represent one standard deviation in terms of least units cited.
[a] Calculated by difference from 100% total.
[b] Total H_2O may represent contributions from O–H, N–H, C–H and H_2.
[c] Uncertainties reflect 2 sigma standard error of a single analysis.
[d] P measurements in silicate melt or metal close to the detection limit.

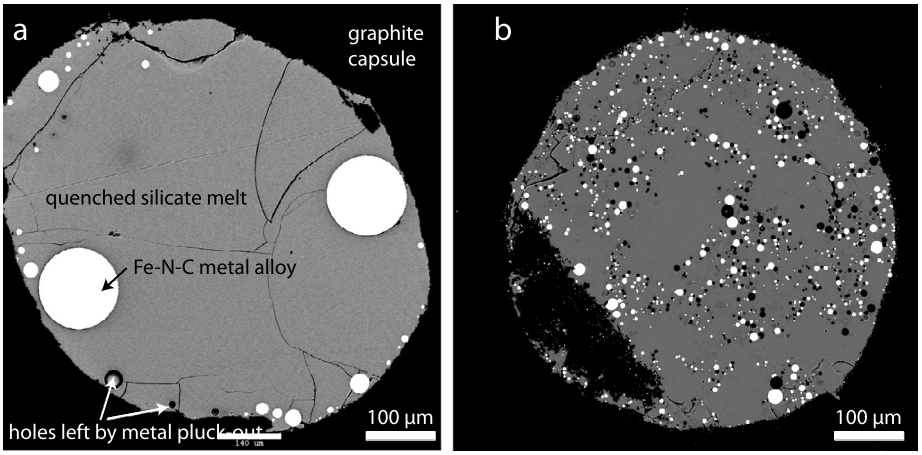

Fig. 1. Back-scattered electron images of samples (a) B706c (ΔIW−0.7, 1.2 GPa, 1400 °C) and (b) B714e (ΔIW−2.3, 3 GPa, 1600 °C). Both samples consist of quenched silicate glass and small spheres of quenched metallic alloy. The holes evident in the images were caused by plucking of metal spheres from the glass during polishing, and are not inferred to indicate vapor saturation.

metallic phase (Fig. 1). Three samples, B690, B693 and B707c, have some minor quench crystallization clustered among the metal domains (too small to be analyzed). Depending on f_{O_2}, the metallic phase forms variable abundances of domains about 10 to 200 µm in diameter (Fig. 1). Most samples exhibited textures appropriate for analysis by SIMS (Fig. 1a), except highly reduced samples (<ΔIW−2.5) such as B714e (Fig. 1b), in which metal domains were finely disseminated throughout the glass.

Most of the Fe–C–N alloys are compositionally homogeneous on the scale of EPMA analyses (~2 µm) (Supplementary material Table S1). Along with Fe and N in the alloys, Al, Ca, P and Si were also measured by EPMA; Si, Ca and Al were analyzed in part to ensure against contamination of analyses by unnoticed silicate, and in all cases Si was below 0.035 wt.% (close or below the detection limit of 0.02 wt.%) and Ca and Al were below their detection limit (of 0.02 wt.%). Phosphorus content generally increases with

Please cite this article in press as: Dalou, C., et al. Nitrogen and carbon fractionation during core–mantle differentiation at shallow depth. Earth Planet. Sci. Lett. (2016), http://dx.doi.org/10.1016/j.epsl.2016.10.026

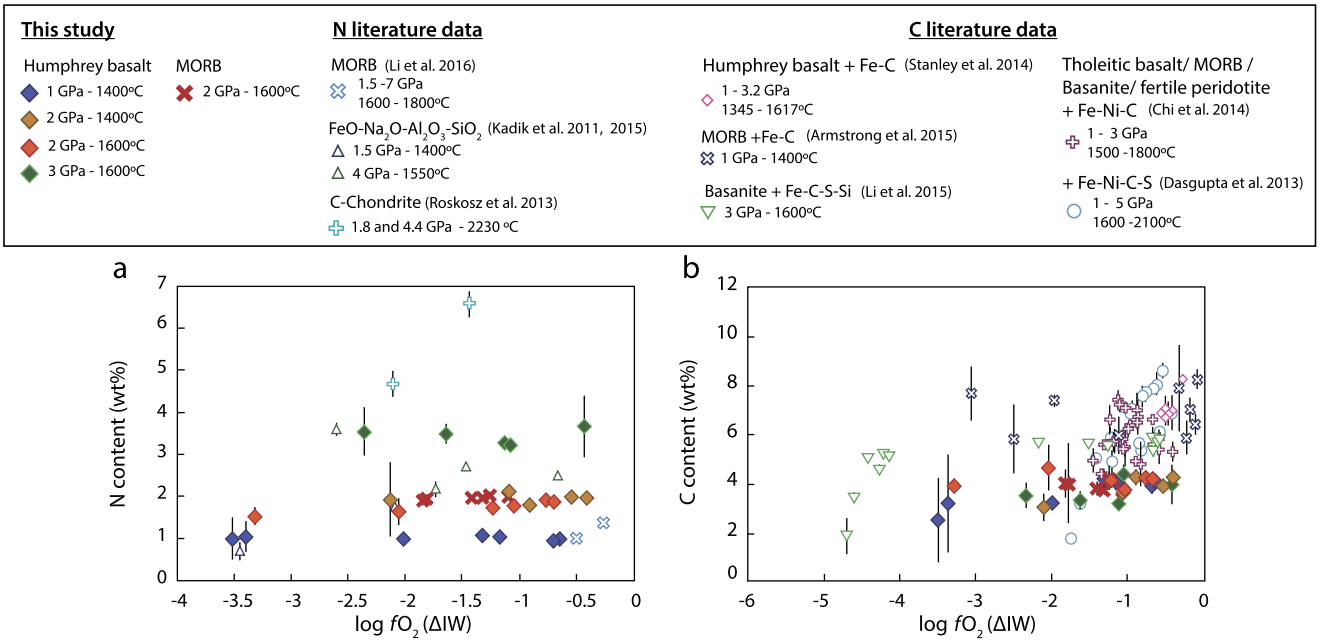

Fig. 2. (a) N contents and (b) C contents in quenched Fe–N–C liquid metal alloy as a function of f_{O_2}. The f_{O_2} values of literature data have been recalculated based on the same "ε formalism" (Wade and Wood, 2005) used to assess γ_{Fe}^{alloy} in the present experiments.

decreasing f_{O_2}, ranging from 0.02 ± 0.01 wt.% (B702b, ΔIW-0.4) to 0.62 ± 0.48 wt.% (B699b, ΔIW-2.12) in experiments starting with Humphrey basalt. In very reduced samples ($<\Delta$IW-2), metal domains show intergrowth of Fe–C–N and Fe–P–N (Fig. S1), interpreted to be textures developed during quench caused by Fe–C and Fe–N alloy segregation (Paju et al., 1988). These features were accounted for in the measurements of N and calculations of C contents in the metal alloy domains (see Supplementary text). Alloy carbon contents were determined by difference from 100 wt.% totals (Table 2) and show that our Fe–C–N alloys are C saturated. This explains why nearly no Si was present and validates Eq. (1).

Silicate melts quenched to chemically homogeneous glasses that are, in most cases, large pools well separated from metal domains. No bubbles were observed, suggesting that neither C nor N saturation was attained during the experiments. Melt compositions determined by EMPA are presented in Supplementary Table S2. As f_{O_2} decreases, melt SiO_2 contents increase owing to oxidation of added Si_3N_4 (Eq. (1)), and FeO melt contents decrease because of Fe-rich metal precipitation, such that the most reduced melts have ~1 wt.% FeO.

3.2. Oxygen fugacity calculations

The oxygen fugacity of each sample (Table 1) is estimated from the equilibrium

$$\underset{\text{alloy}}{\text{Fe}} + \frac{1}{2}O_2 = \underset{\text{silicate melt}}{\text{FeO}}. \quad (2)$$

Following this equilibrium, the f_{O_2} can be calculated from the Fe and FeO concentrations of coexisting alloy and silicate melt from the relation

$$\log_{10} f_{O_2} = \frac{2}{\ln(10)}\left[\ln\left(\frac{X_{FeO}^{melt}}{X_{Fe}^{alloy}}\right) - \ln\left(\gamma_{Fe}^{alloy}\right) + \ln\left(\gamma_{Fe}^{melt}\right) - \ln K\right] \quad (3)$$

(Médard et al., 2008) where X_{FeO}^{melt} and X_{Fe}^{alloy} are the mole fraction of FeO and Fe in the silicate melt and the metal alloy, respectively, calculated on a cation basis; γ_{FeO}^{melt} and γ_{Fe}^{alloy} are the activity coefficients of FeO in the silicate melt and Fe in the metal alloy, respectively; and K is the equilibrium constant of the reaction. Following Médard et al. (2008), we assume γ_{FeO}^{melt} is unity and adopt their empirically calibrated equilibrium constant K. To account for the effect of N and C on γ_{Fe}^{alloy}, we use a derived version of the "Wagner ε formalism" (Wagner, 1962) for non-ideal interactions in liquid Fe alloys, following the approach and formulation of Wade and Wood (2005) and utilizing the calculator provided at http://www.earth.ox.ac.uk/~expet/metalact/. To allow direct comparison to the IW buffer (as presented in Table 2), which is referenced to solid Fe metal, we adjusted the activity of Fe following the method of Stanley et al. (2014)

$$a_{\text{Fe alloy}}^{\gamma\text{Fe}} = a_{\text{Fe alloy}}^{\text{alloy}} + \exp\left(\frac{\Delta S(T - T_L)}{RT}\right) \quad (4)$$

and the resulting f_{O_2} calculated from equations (3) and (4) was compared to the IW buffer determined following Zhang et al. (2016).

3.3. N and C content in molten Fe alloy and silicate glasses

3.3.1. N and C in molten Fe alloy

Nitrogen contents of molten Fe–N–C alloys vary from 0.96 ± 0.04 to 3.7 ± 0.7 wt.%, and are comparable to concentrations reported previously by Kadik et al. (2011, 2015; 0.7–4.4 wt.% at 1.5 and 4 GPa), (Li et al., 2016; 1.0–6.7 wt.% at 1.5 and 7 GPa) in Fe–C–N alloy, and Roskosz et al. (2013; 4.7 and 6.6 wt.% at 1.8 and 4.4 GPa, respectively) in Fe–Ni–N alloy. At a given temperature and pressure, the N contents in the Fe–C–N alloys do not vary with f_{O_2} or melt composition within analytical uncertainty (Fig. 2a). A 200 °C increase at constant pressure decreases N content ~18%, from 1.9 ± 0.9 wt.% to 1.6 ± 0.3 wt.%. At 1400 °C, a 1 GPa increase (from 1.2 to 2.2 GPa) increases N content by 97%, and at 1600 °C (from 2 to 3 GPa) by 83%. The observed effect of pressure on N content in molten alloy is in agreement with the previous studies cited above.

Carbon contents in molten Fe–N–C alloys are between 2.6 ± 1.7 and 4.6 ± 0.9 wt.%, which are comparable to reported contents in graphite-saturated Fe–C ± N ± Ni ± S alloys (e.g. Dasgupta et al.,

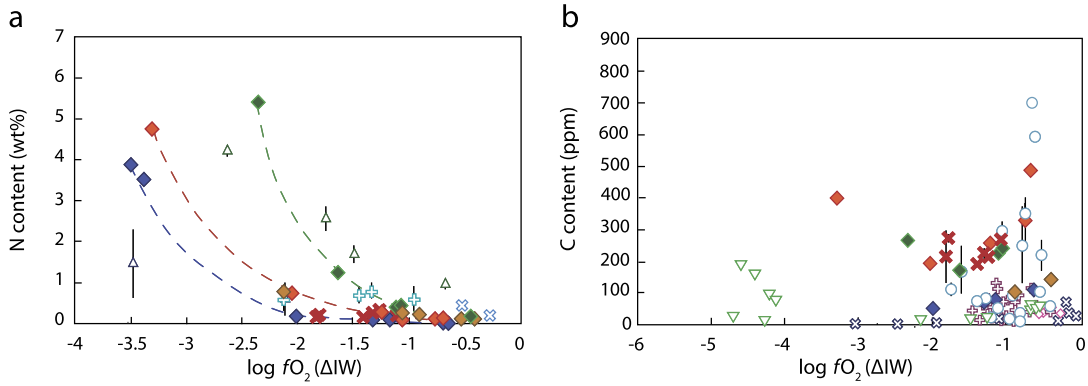

Fig. 3. (a) N contents and (b) C contents of quenched silicate glasses as a function of f_{O_2}. N and C contents in quenched glasses depend chiefly on f_{O_2}, owing to the effect of oxygen fugacity on the speciation of N and C dissolved in silicate melts (see text). Symbols for literature data are the same as in Fig. 2.

2013; Chi et al., 2014; Stanley et al., 2014; Armstrong et al., 2015; Kadik et al., 2015; Li et al., 2015). Graphite-saturated Fe-rich alloy does not show appreciable variations with f_{O_2}, pressure, temperature, or starting composition over the range of conditions in the present study.

3.3.2. N and C in silicate glasses

Nitrogen concentrations in quenched silicate glasses vary significantly, from 0.04 ± 0.005 to 5.42 ± 0.01 wt.%. This range is consistent with previously reported N contents from Kadik et al. (2011, 2015) in FeO–Na_2O–Al_2O_3–SiO_2 glasses, Li et al. (2016) in MORB glasses and Roskosz et al. (2013) in ultramafic glasses (Fig. 3a). Concentrations of N in Humphrey and MORB basaltic glasses increase with decreasing f_{O_2}, in agreement with Libourel et al. (2003), who observed an increase of N solubility in basaltic glass with decreasing f_{O_2} below the IW buffer. In reduced glasses (ΔIW−2), N concentrations are not influenced significantly by a change of 200 °C (0.79 ± 0.02 wt.% versus 0.78 ± 0.04 wt.%, at 1400 °C and 1600 °C respectively). At 1600 °C and ΔIW ∼−2, the observed N content increases from 0.78 ± 0.01 wt.% at 2 GPa to 5.42 ± 0.01 wt.% at 3 GPa. Finally, for the experiments analyzed in this work, melt composition has no clear effect on N concentrations; observed N in Humphrey basalt and MORB glasses are not distinguishable (0.26 ± 0.01 and 0.26 ± 0.01wt.%, respectively at 2 GPa, 1600 °C, and ΔIW−1.3).

The C contents in silicate glasses also vary significantly with f_{O_2}: from 49 ± 3 to 487 ± 1 ppm. Although this range is similar to that documented by Dasgupta et al. (2013) in tholeiitic basalt, MORB, basanite and peridotitic melts, it is greater than concentrations observed by Li et al. (2015), Chi et al. (2014), Stanley et al. (2014) and Armstrong et al. (2015) for conditions more reduced than IW. All of these studies measured C contents less than 200 ppm in the silicate melt regardless of P, T, or melt compositions. Temperature affects C contents in silicate melts and also modifies the influence of f_{O_2} on C content. At 1400 °C, C contents decrease from 141 ± 11 ppm at ΔIW−0.4 to 49 ± 3 ppm at ΔIW−2. At 1600 °C, C content decreases from 487 ± 1 to 166 ± 9 ppm between ΔIW−0.7 and ΔIW−1.6, and then increases to 401 ± 7 ppm at ΔIW−3.3.

3.4. N and C partition coefficients between molten Fe alloy and silicate glasses

Table 2 and Figs. 4 and 5 report molten alloy/silicate melt partition coefficients for N and C ($D_N^{metal/silicate}$ and $D_C^{metal/silicate}$) calculated from averaged concentrations and their associated standard deviation ($1\sigma_{SD}$) of 2–5 analyses per sample. Phosphorus partition coefficients between molten alloy and silicate melt ($D_P^{metal/silicate}$) are also reported. Although the uncertainties are high on some of these values (e.g., for samples in which P is near the detection limit in either the metal or glass), P becomes more siderophile at more reducing conditions, in agreement with Righter (2003; and the references therein). Because the stability of N in silicate melt increases at more reducing conditions (Fig. 3a), $D_N^{metal/silicate}$ decreases from 24 ± 3 to 0.32 ± 0.04 with decreasing f_{O_2} ($-0.4 < \Delta IW < -3.5$). At highly reduced conditions, below ΔIW−2.3, $D_N^{metal/silicate} < 1$, i.e. N becomes lithophile rather than siderophile. Despite differences in melt composition, P, and T, variations of $D_N^{metal/silicate}$ with f_{O_2} from experiments in this study are consistent with those determined previously (Kadik et al., 2011, 2015; Li et al., 2016; Roskosz et al., 2013).

For variations in intensive variables explored in this and previous studies, oxygen fugacity has, by far, the largest influence on $D_N^{metal/silicate}$. But in detail, under comparable conditions, values of $D_N^{metal/silicate}$ determined by Kadik et al. (2011, 2015) are lower while those determined by Roskosz et al. (2013) are marginally higher than those determined for basalt in the present study. At low $f_{O2,}$ N is dissolved chiefly as N–H species, NH_2, NH_3 and/or NH_4 (Mysen and Fogel, 2010; Kadik et al., 2015). Therefore, its solubility increases with the increasing OH content dissolved in the silicate melt. Kadik et al. (2015) report H_2O contents in silicate melt of 1.7 to 2.9 wt.%, i.e. two to four times greater than those in the present study (Table 2), and this may account for the greater concentration of N in silicate in their experiments (Fig. 4a). An additional effect may arise between studies owing to difference in C content of metallic alloys, as dissolved C decreases N solubility in metals (e.g. Siwka, 2008). On average, C contents in our metal alloys are ∼4 wt.%, while metal alloys in Roskosz et al. (2013), which have more than twice the N of those reported in the present study, are C-free (Fig. 3a).

At similar f_{O_2}, $D_N^{metal/silicate}$ decreases with increasing temperature and pressure, in agreement with Kadik et al. (2015). With increasing pressure, Li et al. (2016; 1.5–7 GPa) and, over a larger pressure interval (1.8–14.8 GPa), Roskosz et al. (2013), found $D_N^{metal/silicate}$ to increase between Fe–C–N and Fe–Ni–N alloy, respectively, and silicate melt. However, recalculation using the Wade and Wood (2005) algorithm that accounts for the effect of N and Ni in on the activity of Fe, assuming that interaction parameters are not pressure-dependent (Wade and Wood, 2005), shows that f_{O_2} increases from ΔIW−2.1 at 1.8 GPa to ΔIW−0.9 at 14.8 GPa in the experiments by Roskosz et al. (2013). Therefore, the apparent effect of pressure may chiefly result from the accompanying influence of f_{O_2}. Similarly, the effect of changing f_{O_2} (from ΔIW−0.5 at 1.5 GPa to ΔIW+0.6 at 7 GPa) in Li et al. (2016) obscures the effect of pressure on $D_N^{metal/silicate}$.

Please cite this article in press as: Dalou, C., et al. Nitrogen and carbon fractionation during core–mantle differentiation at shallow depth. Earth Planet. Sci. Lett. (2016), http://dx.doi.org/10.1016/j.epsl.2016.10.026

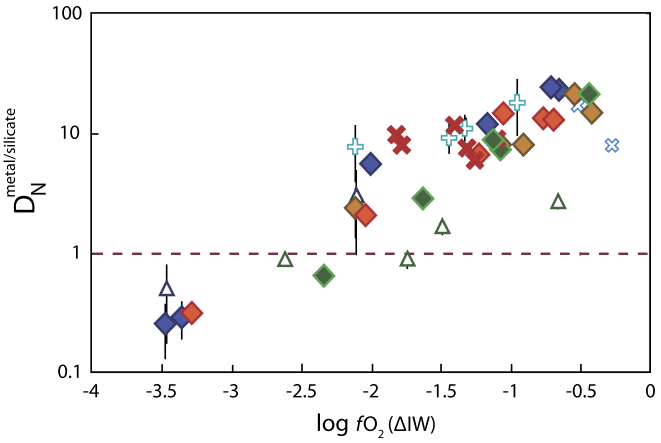

Fig. 4. $D_N^{metal/silicate}$ as a function of f_{O_2}. Also plotted for comparison are previously experimentally determined values of $D_N^{metal/silicate}$ from Li et al. (2016), Roskosz et al. (2013) and Kadik et al. (2011, 2015), with values of f_{O_2} recalculated as discussed in Fig. 2. Note that melt composition and P–T conditions have little effect on $D_N^{metal/silicate}$ and that variations chiefly depend on changing f_{O_2}.

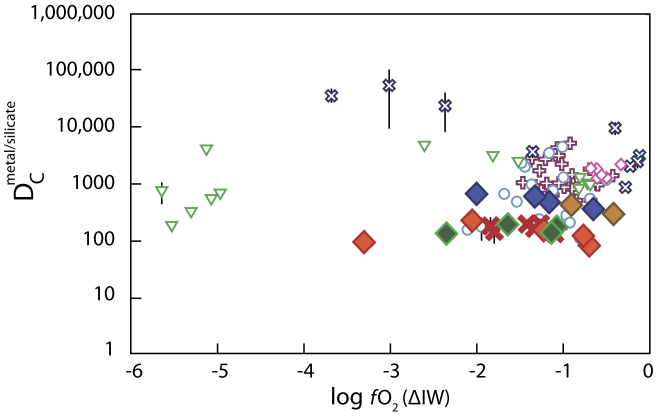

Fig. 5. $D_C^{metal/silicate}$ as a function of f_{O_2}. The f_{O_2} of experiments from the literature have been recalculated using the formalism described in Wade and Wood (2005).

Because the C content of graphite-saturated molten alloy varies little (Fig. 3b), $D_C^{metal/silicate}$ is controlled chiefly by the influence of f_{O_2} and other variables on C concentrations in graphite-saturated silicate melt (Fig. 5). At 1400 °C, $D_C^{metal/silicate}$ increases from 300 ± 30 to 670 ± 50 with decreasing f_{O_2} (from ΔIW−0.4 to ΔIW−3.5) and is higher than at 1600 °C. At 1600 °C, $D_C^{metal/silicate}$ increases from 87 ± 3 to 240 ± 50 between ΔIW−0.7 and ΔIW−2.1, and then decreases to 99 ± 6 at ΔIW−3.3. Similar increases in $D_C^{metal/silicate}$ with decreasing f_{O_2} were documented by Li et al. (2015) and Armstrong et al. (2015) in experiments from ΔIW−0.8 to ΔIW−3. Their results also show that the trend does not continue at very reducing conditions, as values of $D_C^{metal/silicate}$ at ΔIW−4 to ΔIW−5 are comparable to or possibly lower than those at ΔIW−2.5 to ΔIW−3. At more modestly reduced conditions (e.g., near ΔIW−1.5), the scatter of $D_C^{metal/silicate}$ results chiefly from the effects of large NBO/T variation in the melts (e.g., Dasgupta et al., 2013; Chi et al., 2014). Additionally, Armstrong et al. (2015) found higher values of $D_C^{metal/silicate}$ than those from the present study at comparable f_{O_2}. This discrepancy may be attributable to differences in hydrous species and related in part to the availability of CH_4, owing to the potential for C to dissolve as CH_4 under reducing conditions (Ardia et al., 2013; Dasgupta et al., 2013; Armstrong et al., 2015). Under dry conditions (H_2O < 0.1 wt.%, Armstrong et al., 2015), C solubility in silicate melts is inhibited,

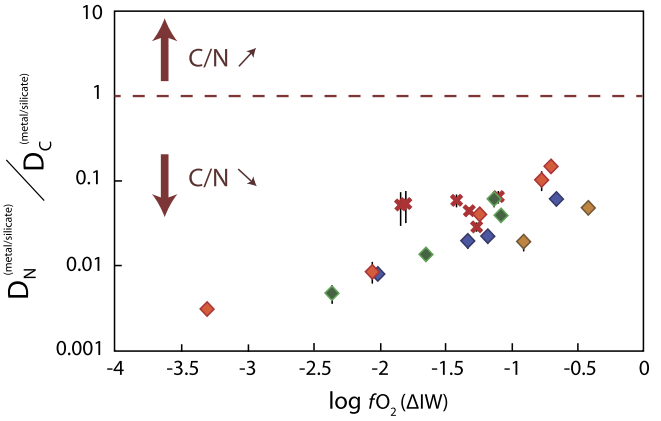

Fig. 6. $D_N^{metal/silicate}/D_C^{metal/silicate}$ as a function of f_{O_2}. $D_N^{metal/silicate}/D_C^{metal/silicate}$ decreases with decreasing f_{O_2} and is lower than unity, regardless of f_{O_2}, melt composition, or P and T conditions. Therefore, the C:N ratio of silicate melts decreases during core–mantle differentiation (see text).

resulting in increased $D_C^{metal/silicate}$ (Fig. 3b). In addition, higher C contents in the silicate melt are observed at higher temperature, perhaps owing to stabilization of CH_4, although a strong temperature effect for CH_4 solubility in silicate melts has not been demonstrated previously.

The simultaneous determination of $D_N^{metal/silicate}$ and $D_C^{metal/silicate}$ from the same experiments allows evaluation of their relative values over a large span of f_{O_2} (Fig. 6). At all conditions examined, $D_C^{metal/silicate}$ is markedly greater (87 ± 3 to 670 ± 50) than $D_N^{metal/silicate}$ (0.32 ± 0.04 to 24 ± 3), and $D_N^{metal/silicate}/D_C^{metal/silicate}$ is much less than 1 in all cases. Owing to progressively more lithophile behavior of N, fractionation of C from N during alloy-silicate equilibration becomes more extreme (<0.001) under reducing conditions (Fig. 5)

4. Discussion

4.1. Metal/silicate partitioning and the sequestration of N in the core

The values of $D_N^{metal/silicate}$ measured to date indicate modestly siderophile behavior of N under a wide range of conditions, affirming previous suggestions that the core could be a major repository of Earth's N (Marty, 2012; Roskosz et al., 2013; Johnson and Goldblatt, 2015; Li et al., 2016). However, the magnitude of the core N reservoir depends on a number of factors, including the conditions of metal–silicate equilibration as well as the dynamical processes influencing volatile and siderophile elements during early planetary differentiation.

Modern models of metal–silicate equilibration during core formation acknowledge the likelihood that f_{O_2} evolved throughout the process. They include scenarios in which the f_{O_2} began at strongly reducing (~IW−4; Rubie et al., 2011) to modestly oxidizing conditions (~IW−1; Siebert et al., 2013), but agree that the process converged to near IW−2, as dictated by equilibration of Fe-rich metal with silicate containing 8 wt.% FeO* (total Fe as FeO), similar to the modern mantle (McDonough and Sun, 1995). For core sequestration of N and other volatiles, the important constraint is not the evolution of f_{O_2} during the entire history of metal–silicate reaction, but only the f_{O_2} during the interval in which the predominant fraction of volatiles was present. For example, if volatiles were delivered early (Sarafian et al., 2014), then f_{O_2} matters throughout the entire history of core formation, but if a greater portion of the volatiles were added to

Please cite this article in press as: Dalou, C., et al. Nitrogen and carbon fractionation during core–mantle differentiation at shallow depth. Earth Planet. Sci. Lett. (2016), http://dx.doi.org/10.1016/j.epsl.2016.10.026

Earth during the later stages of accretion (Morbidelli et al., 2000) then the f_{O_2} prevailing during earlier stages has little influence on core storage of these elements. Moreover, much of the metal present in the core likely did not equilibrate with the volatiles delivered to the protomantle, either because the metal was already in the core at the time of volatile delivery (Hirschmann, 2016) or because the core-destined metal may not have equilibrated fully with the entire mass of the mantle (Deguen et al., 2014; Rubie et al., 2015).

For the extreme plausible conditions of metal–silicate equilibration, ranging from IW−3.5 (Rubie et al., 2011) to IW−1 (Siebert et al., 2013) the applicable values of $D_N^{metal/silicate}$ are 0.2 and 10, respectively (Fig. 4). For the limiting case in which the entire core and mantle equilibrate (momentarily ignoring the role of other sinks, such as the atmosphere or loss to space), these limits permit the fraction of Earth's N in the core to be between 10 and 90%. For conditions near IW−2, more applicable to the late stages of accretion, core formation, and volatile delivery, the corresponding value of $D_N^{metal/silicate}$ is near 2 (Fig. 4), which would place 50% of terrestrial N in the core for total core/mantle equilibration. If only one third of the core metal equilibrated with the volatile inventory delivered to the protomantle, then this amount is reduced to 25%. We emphasize that even these modest values ignore the formation of an atmosphere overlying the accreting partially molten Earth, which has the effect of diminishing the fraction of terrestrial volatiles available to the core (Hirschmann, 2016). Thus, the core could be the major repository of terrestrial N only for extremely efficient core–mantle equilibration scenarios in which median segregation conditions were more reduced than the normative value of IW−2. An important caveat is that these arguments do not account for the possibility that quite different values of $D_N^{metal/silicate}$ prevail at the high P, T, and melt compositions characteristic of terrestrial core formation, which is discussed further in Section 4.4 below.

4.2. Fractionation of C/N by core formation

As discussed in the Introduction, it has been proposed that the high C:N ratio of the BSE could be a product of sequestration of N in the core (Marty, 2012; Roskosz et al., 2013), but such scenarios require the preference of core-forming metal for N to exceed that for C. Previous comparisons between experimentally determined values of $D_N^{metal/silicate}$ and $D_C^{metal/silicate}$ have led to the inference that core formation should have the opposite consequences (Tucker and Mukhopadhyay, 2014; Bergin et al., 2015; Hirschmann, 2016), producing a BSE with a low C:N ratio compared to plausible cosmochemical sources. However, these estimates were derived from a combination of separate studies of C and N partitioning that were conducted at similar but not directly comparable conditions and a value of $D_N^{metal/silicate}$ equal to 20 from Roskosz et al. (2013) was used in all the models, regardless of the considered f_{O_2}. Our simultaneous determination of $D_N^{metal/silicate}$ and $D_C^{metal/silicate}$ (Fig. 6) and the refinement of the effect of f_{O_2} on $D_N^{metal/silicate}$ (Fig. 4) indicates that removal of metal to the core should greatly reduce the C:N ratio of residual silicates, and that the magnitude of this reduction would be enhanced under more reducing conditions. Thus, based on available experimental data, metal–silicate partitioning in a shallow magma ocean fails to explain the high C/N of the BSE, and any effects of core formation on BSE volatiles require yet greater relative loss of N by an additional process, such as atmospheric escape (Tucker and Mukhopadhyay, 2014; Bergin et al., 2015) or accretion of planetesimals with C/N enhanced by processes on those parent bodies (Hirschmann, 2016).

Table 3
Variables used in the mass calculation (Fig. 6) detailed in Appendices A, B.

	$\log f_{O_2}$ (ΔIW−)	Average solubility S_i (ppm/MPa)	Partition coefficients $D_i^{metal/silicate}$
C	0.5–1	0.22	100
	1.8–2.2	0.10	250
	3.4–3.6	0.17	2000
N	0.7–1	0.7	20
	1.8–2.2	3	5
	3.4–3.6	26	0.3

4.3. Effects of atmospheric loss

The effects of atmospheric loss are potentially complex, as they depend on the timing and energetics of loss events as compared to the evolution of the volatile inventory. For example, quite different effects could result depending on whether ablation occurs from a high temperature thick atmosphere (Tucker and Mukhopadhyay, 2014) or a low temperature, less massive atmosphere (e.g. De Niem et al., 2012; Schlichting et al., 2015). Yet different effects would be expected from a giant impact of sufficient energy to ablate not just a pre-existing atmosphere but also significant fractions of a vaporized mantle (Pahlevan and Stevenson, 2007). Here we consider only a simple scenario in which the Earth loses a thick atmosphere developed atop a magma ocean, similar in composition and mass to those evaluated previously by Hirschmann (2016; and the references therein). In comparison, high energy removal from a giant impact is less capable of fractionating N from C, and low temperature removal during accretion of a late veneer or a late heavy bombardment could feasibly remove N preferentially compared to C (Schlichting et al., 2015), but alternatively could accumulate more volatiles than are ablated (De Niem et al., 2012).

The combined effects of core formation and removal of an atmosphere developed over a magma ocean on the C:N ratio of the non-metallic Earth can be modeled following the procedure of Hirschmann (2016). Here, we refine that calculation using newly determined values for $D_N^{metal/silicate}$ and $D_C^{metal/silicate}$, which vary significantly with f_{O_2} of the magma ocean. Additional parameters required for the calculation are summarized in Table 3. As shown in Fig. 7, core–mantle differentiation followed by atmospheric loss diminishes the C:N ratio of the non-metallic Earth during magma-metal equilibration, regardless of whether the conditions are oxidized or reduced (graded bars). In the case of highly reduced conditions, N is more soluble than C in silicate melt (Table 3) and so magma ocean degassing followed by atmospheric loss further diminishes C/N of the non-metallic Earth. For less reducing conditions, C solubility can exceed that of N, but the magnitude of C/N fractionation associated with atmosphere formation and loss is insufficient to overcome the strong decrease in C/N brought about by core formation (Fig. 7).

4.4. Extrapolation to more extreme core-forming conditions

The preceding discussion is based on a body of experimental measurements for $D_N^{metal/silicate}$ which are at lower temperatures and pressures, and, in most cases, less magnesian melt compositions, than those applicable to core formation on the Earth. More comprehensive exploration of the effects of these variables on $D_N^{metal/silicate}$ and $D_N^{metal/silicate}/D_C^{metal/silicate}$ is desirable, in particular because $D_C^{metal/silicate}$ is known to diminish significantly for less polymerized melt compositions (Dasgupta et al., 2013; Armstrong et al., 2015). However, the available data (Fig. 4) suggest that the chief influence on $D_N^{metal/silicate}$ is f_{O_2}, and that the effects of T, P, and melt composition are subordinate in the range of pressure investigated. At pressures between 4 and 20 GPa, and

Please cite this article in press as: Dalou, C., et al. Nitrogen and carbon fractionation during core–mantle differentiation at shallow depth. Earth Planet. Sci. Lett. (2016), http://dx.doi.org/10.1016/j.epsl.2016.10.026

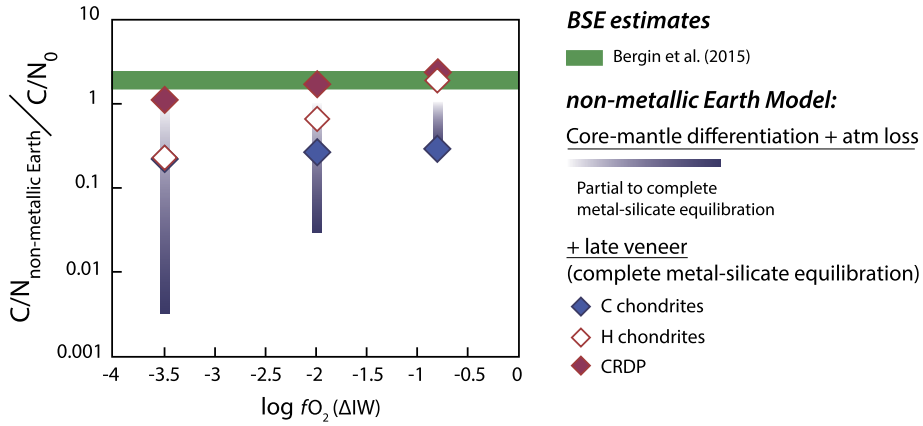

Fig. 7. Comparison of the C:N ratio of the modern BSE (green rectangles) with model calculations of C/N fractionation. The model first fractionates volatiles on a chondritic Earth by core formation, loses the early atmosphere to space (graded bars), and then incorporates a chondritic late veneer using the C/N of carbonaceous chondrites (blue diamonds), or a C-rich late veneer using type H ordinary chondrites (white diamonds) and C-rich differentiated planetesimals (CRDP; see text; red diamonds). More details on the model can be found in the main text and in Appendices A, B. (For interpretation of the references to color in this figure legend, the reader is referred to the web version of this article.)

temperatures up to 2800 °C, Roskosz et al. (2013) show that N solubility in metal increases with increasing P. However, as noted above, much of this variation is likely owing to a secular increase in f_{O_2} with pressure in their experiments. At higher P–T conditions (>10 GPa, Gessmann et al., 2001), Si becomes siderophile (>1 wt.% in metal alloy). The influence of Si on $D_N^{metal/silicate}$ and $D_C^{metal/silicate}$ is not yet constrained, but it may affect N and C solubility in core-forming metal alloy differentially. The effect of silicate melt composition may also be distinct. $D_C^{metal/silicate}$ decreases with decreasing melt polymerization (Dasgupta et al., 2013), whereas $D_N^{metal/silicate}$ may be comparatively less affected (e.g., comparing $D_N^{metal/silicate}$ values for "chondritic" melts from Roskosz et al. (2013) with those from basalt in the present study, Fig. 4). Therefore, values of $D_N^{metal/silicate}/D_C^{metal/silicate}$ applicable to ultramafic magma ocean silicate compositions may be larger than those depicted in Fig. 6, but should remain smaller than unity, as applicable values of $D_C^{metal/silicate}$ remain above 100 (Dasgupta et al., 2013; Chi et al., 2014; Armstrong et al., 2015), higher than any values yet documented for $D_N^{metal/silicate}$ at conditions suitably reducing for core formation.

4.5. The role of parent body processes and the late veneer

The apparent failure of core formation, with or without atmospheric loss, to account for the BSE C:N ratio raises questions about the C:N ratios of materials accreted to the Earth. The calculations above assumed that material supplied to the accreted Earth had C:N ratios similar to those of CI carbonaceous chondrites, which are similar to C:N ratios in other primitive cosmochemical materials such as enstatite chondrites and many ordinary and carbonaceous chondrites (e.g., Bergin et al., 2015; Hirschmann, 2016). However, some of the ordinary and carbonaceous chondrite compositions reviewed by Bergin et al. (2015) and Hirschmann (2016) have C:N ratios much greater than that of the BSE, and a simple *ad hoc* explanation is that Earth happened to accrete from materials more similar to these. This hypothesis deserves further exploration through improved understanding of volatile behavior during parent body processing and accretion.

The C:N ratio of the non-metallic Earth may also be greatly influenced by accretion of a late veneer following removal of metal to the core and the cessation of large-scale volatile-loss events. Based on the abundances of platinum-group elements (PGE), the mass of the late veneer is thought to amount to ~0.3% of the Earth (e.g., Walker, 2009), and is commonly considered to be an appreciable source of Earth's volatiles (e.g., Albarede, 2009). Addition of a late veneer similar to carbonaceous chondrites (e.g. Wang and Becker, 2015) would raise the overall volatile budget of the non-metallic Earth, but would not produce a C:N ratio similar to the BSE (blue diamonds in Fig. 7). An alternative scenario explored by Hirschmann (2016) is that a fraction of the late veneer consisted of differentiated bodies with high C:N ratios. Examples of such objects include CO and CV chondrites from the compilation of Kerridge (1985) (C/N = 129 ± 53 and 136 ± 54), H ordinary chondrites compiled by Bergin et al., 2015 (C/N= 390 ± 250), and ureilite achondrites (C/N= 1000 ± 600; Downes et al., 2015). As a demonstration of the potential influence of a C-rich late veneer, we calculate the effect of accreting a mixture consisting of a material with a C:N ratio similar to H ordinary chondrites (C/N = 390; white diamonds on Fig. 7) versus a material made of C-rich differentiated planetesimals (CRDP). The C:N ratio of the CRDP (red diamonds on Fig. 7) is composed of a mixture of 30% of a material with a C:N ratio of 23, similar to CI, and 70% of a material with a C:N ratio of 1000, similar to ureilite. We emphasize that these are example calculations to explore accretion of differentiated C-rich bodies, and are not meant as models tied to the comprehensive compositions of specific meteorite classes. The origin of parent bodies with high C/N presumably requires some combination of melting, metamorphism, or aqueous alteration under conditions that can retain refractory C whilst liberating N, and the diversity of meteorite objects that have elevated C/N (CO, CV, and H chondrites, ureilites) suggests that objects in the solar system may have had broadly similar characteristics. Combined with the effects of core formation and atmospheric loss, both scenarios produce non-metallic Earth ratios approaching that of the BSE, though the latter mixture is most similar.

5. Conclusions

Determinations of $D_N^{metal/silicate}$ between Fe-rich alloy and basaltic melt over a large range of f_{O_2} (ΔIW−0.4 to −3.5) reveal that N is mildly siderophile for modestly reducing oxygen fugacities and becomes lithophile under strongly reduced conditions. The decrease in $D_N^{metal/silicate}$ results from an increase of N solubility in silicate melts towards reduced conditions. The modest preference of N for metallic alloy indicates that the core is a significant but not dominant reservoir of terrestrial N.

N is less siderophile than C under all conditions investigated and if this relationship is applicable to the full range of tempera-

Please cite this article in press as: Dalou, C., et al. Nitrogen and carbon fractionation during core–mantle differentiation at shallow depth. Earth Planet. Sci. Lett. (2016), http://dx.doi.org/10.1016/j.epsl.2016.10.026

tures, pressures, and phase compositions applicable to core formation, then such a process must have lowered the C:N ratio of the non-metallic Earth. Mass balance modeling suggests that this effect cannot be reversed by loss of an atmosphere to space, and together these considerations point to an important role for C/N fractionation on parent bodies prior to accretion to the Earth. Improved understanding of the fate of C and N during planetesimal differentiation and accretion is required to identify the origin of Earth's characteristic depletion in N compared to carbonaceous chondritic reference materials.

Acknowledgements

This work was supported by NSF AST1344133 to M.M.H. SIMS analyses were obtained with the help of Richard Hervig and Lynda Williams at the ASU National SIMS facility, supported by NSF EAR0948848. We also acknowledge helpful comments by A. Sarafian and two anonymous reviewers and editorial handling of the manuscript by B. Marty.

Appendix A. Mass balance calculation

The C:N ratios of the non-metallic Earth in Fig. 7 (graded bars and diamonds) were calculated from the mass balance calculation of Hirschmann (2016). Model results were calculated for a slightly reduced (ΔIW-0.7 to -0.9), reduced (ΔIW-1.8 to -2.2), and very reduced (ΔIW-3.4 to -3.6) magma ocean (Table 3).

The total mass of C and N in the bulk silicate Earth, $M_{CorN}^{\text{silicate}}$, is calculated from:

$$M_i^{\text{silicate}} = C_i^{\text{silicate}} \cdot m_i^{\text{silicate}}, \tag{A.1}$$

where m_i^{silicate} is the mass of the magma ocean (amounting to the current mass of the mantle, 4×10^{27} g), and C_i^{silicate} is the volatile concentration in the bulk silicate Earth derived from:

$$C_i^{\text{silicate}} = S_i \cdot P_i. \tag{A.2}$$

The solubilities of element i in silicate melt, S_i, for C and N are given in Table 3 for each f_{O_2} range. The vapor partial pressure, P_i, is found from:

$$P_i = r \cdot M_i^{\text{atmosphere}} \cdot g/A, \tag{A.3}$$

where the constants r, g, and A are respectively the mass ratio between the volatile species and the element of interest (e.g. $r = 44/12$ for CO_2 vapor, but unity for N_2 vapor), gravitational acceleration (9.8 m/s^2), and the surface area of the planet (5.1×1014 m^2). The total mass of element i in the atmosphere, $M_i^{\text{atmosphere}}$, is:

$$M_i^{\text{atmosphere}} = \frac{M_i}{(S_i \cdot r \cdot g/A) \cdot (m_i^{\text{silicate}} + D_i^{\text{metal/silicate}} \cdot m_i^{\text{metal}}) + 1}, \tag{A.4}$$

where M_i is the total mass of the volatile component i and m_i^{metal} is the total mass of the alloy equilibrating with the magma ocean. The partition coefficients between metal alloy and silicate melt, $D_i^{\text{metal/silicate}}$, for C and N are given in Table 3 for each f_{O_2} range. To model core–mantle differentiation and subsequent atmospheric loss, we assume partial to complete equilibration between a mass of silicate (m_i^{silicate}) and a mass of metal alloy. Therefore, the alloy mass is varied from 0 to 2×10^{27} g in the calculation.

In this model, addition of a late veneer (diamonds in Fig. 7) assumes complete equilibration of metal and silicate after core–mantle differentiation and atmospheric loss. We investigate two late veneer compositions: a chondritic and a "C-rich" late veneer. The chondritic late veneer uses a CI composition (Kerridge, 1985) of 35,000 ppm C and 1,500 ppm N (model results represented by blue diamonds in Fig. 7). Two compositions of the "C-rich" late veneer are calculated: the red diamonds show the results for late veneer composed of a mixture of 30% of a material with a C:N ratio (23) similar to CI and 70% of a material with a C:N ratio (1000) similar to ureilite (Downes et al., 2015) with 30,000 ppm C and 30 ppm N; the white diamonds show the results for a late veneer made of a material with a C:N ratio equal to 390, similar to the H ordinary chondrites (CH).

All C:N ratios are normalized to the C:N ratio of a proto-Earth, C/N_0, estimated at 25 (Bergin et al., 2015).

Finally, an estimated C:N ratio of 49 ± 9.3 (Bergin et al., 2015) for the modern BSE is shown in Fig. 7 (green rectangle).

Appendix B. Quantitative X-ray mapping and determination of P contents

At highly reduced conditions, some metal domains show quench textures comprised of an intergrowth of exsolved Fe–C–N and Fe–P–N quenched liquids. We accounted for this heterogeneity either by averaging multiple focused beam analyses or, in the extreme case of B699b (Fig. S1), by collecting quantitative X-ray maps for N, Fe, P and Si using ProbeImage by ProbeSoftware. The X-ray maps were acquired at 15 kV, 150 nA and a dwell time of 1000 ms per pixel. Nitrogen was acquired on two spectrometers (LDE1) and X-ray intensities were aggregated in post-processing. Data were corrected with the MAN background correction method (Donovan et al., 2016), PROZA matrix correction method (Bastin et al., 1998), and FFAST mass absorption coefficients (Chantler et al., 2005) in CalcImage. Quantified X-ray maps were then exported to Surfer software (Golden Software) and regions of interest were chosen for calculating average compositions of metal blobs.

Phosphorus was not directly measured in some metals, as listed in Table S1, as the metals had been inadvertently plucked out during re-polishing following analysis by SIMS and prior to reanalysis. In order to more precisely calculate C contents by difference, we estimated metal P contents for these samples by referencing their measured glass P contents to a regression of glass P contents against metal P contents in other samples. The error on the regression was estimated by conducting a York (1966) fit, taking into account uncertainties in both glass and metal data. The consequent errors (2σ) were then propagated to determine the uncertainty on $D_P^{\text{metal/silicate}}$.

Appendix C. Supplementary material

Supplementary material related to this article can be found online at http://dx.doi.org/10.1016/j.epsl.2016.10.026.

References

Adler, J.F., Williams, Q., 2005. A high-pressure X-ray diffraction study of iron nitrides: implications for Earth's core. J. Geophys. Res., Solid Earth 110 (B1).

Albarede, F., 2009. Volatile accretion history of the terrestrial planets and dynamic implications. Nature 461, 1227–1233.

Ardia, P., Hirschmann, M.M., Withers, A.C., Stanley, B.D., 2013. Solubility of CH_4 in a synthetic basaltic melt, with applications to atmosphere-magma ocean-core partitioning of volatiles and to the evolution of the Martian atmosphere. Geochim. Cosmochim. Acta 114, 52–71.

Armstrong, L.S., Hirschmann, M.M., Stanley, B.D., Falksen, E.G., Jacobsen, S.D., 2015. Speciation and solubility of reduced C–O–H–N volatiles in mafic melt: implications for volcanism, atmospheric evolution, and deep volatile cycles in the terrestrial planets. Geochim. Cosmochim. Acta 171, 283–302.

Aubaud, C., Withers, A.C., Hirschmann, M.M., Guan, Y., Leshin, L.A., Mackwell, S.J., Bell, D.R., 2007. Intercalibration of FTIR and SIMS for hydrogen measurements in glasses and nominally anhydrous minerals. Am. Mineral. 92, 811–828.

Bastin, G.F., Dijkstra, J.M., Heijligers, H.J.M., 1998. PROZA96: an improved matrix correction program for electron probe microanalysis, based on a double Gaussian $\Phi(\rho z)$ approach. X-Ray Spectrom. 27 (1), 3–10.

Bergin, E.A., Blake, G.A., Ciesla, F., Hirschmann, M.M., Li, J., 2015. Tracing the ingredients for a habitable earth from interstellar space through planet formation. Proc. Natl. Acad. Sci. 112, 8965–8970.

Chantler, C.T., Olsen, K., Dragoset, R.A., Kishore, A.R., Kotochigova, S.A., Zucker, D.S., 2005. X-ray Form Factor, Attenuation and Scattering Tables (Version 2.1). National Institute of Standards and Technology, Gaithersburg, MD.

Chi, H., Dasgupta, R., Duncan, M.S., Shimizu, N., 2014. Partitioning of carbon between Fe-rich alloy melt and silicate melt in a magma ocean – implications for the abundance and origin of volatiles in Earth, Mars, and the Moon. Geochim. Cosmochim. Acta 139, 447–471.

Dasgupta, R., 2013. Ingassing, storage, and outgassing of terrestrial carbon through geologic time. Rev. Mineral. Geochem. 75, 183–229.

Dasgupta, R., Buono, A., Whelan, G., Walker, D., 2009. High-pressure melting relations in Fe–C–S systems: implications for formation, evolution, and structure of metallic cores in planetary bodies. Geochim. Cosmochim. Acta 73, 6678–6691.

Dasgupta, R., Chi, H., Shimizu, N., Buono, A.S., Walker, D., 2013. Carbon solution and partitioning between metallic and silicate melts in a shallow magma ocean: implications for the origin and distribution of terrestrial carbon. Geochim. Cosmochim. Acta 102, 191–212.

De Niem, D., Kührt, E., Morbidelli, A., Motschmann, U., 2012. Atmospheric erosion and replenishment induced by impacts upon the Earth and Mars during a heavy bombardment. Icarus 221, 495–507.

Deguen, R., Landeau, M., Olson, P., 2014. Turbulent metal–silicate mixing, fragmentation, and equilibration in magma oceans. Earth Planet. Sci. Lett. 391, 274–287.

Donovan, J.J., Singer, J.W., Armstrong, J.T., 2016. A new EPMA method for fast trace element analysis in simple matrices. Am. Mineral. 101, 1839–1853.

Downes, H., Abernethy, F.A.J., Smith, C.L., Ross, A.J., Verchovsky, A.B., Grady, M.M., Jenniskens, P., Shaddad, M.H., 2015. Isotopic composition of carbon and nitrogen in ureilitic fragments of the Almahata Sitta meteorite. Meteorit. Planet. Sci. 50, 255–272.

Gessmann, C.K., Wood, B.J., Rubie, D.C., Kilburn, M.R., 2001. Solubility of silicon in liquid metal at high pressure: implications for the composition of the Earth's core. Earth Planet. Sci. Lett. 184, 367–376.

Hirschmann, M.M., 2016. Constraints on the early delivery and fractionation of Earth's major volatiles from C/H, C/N, and C/S ratios. Am. Mineral. 101, 540–553.

Johnson, B., Goldblatt, C., 2015. The nitrogen budget of Earth. Earth-Sci. Rev. 148, 150–173.

Kadik, A.A., Kurovskaya, N.A., Ignat'ev, Y.A., Kononkova, N.N., Koltashev, V.V., Plotnichenko, V.G., 2011. Influence of oxygen fugacity on the solubility of nitrogen, carbon, and hydrogen in $FeO–Na_2O–SiO_2–Al_2O_3$ melts in equilibrium with metallic iron at 1.5 GPa and 1400 °C. Geochem. Int. 49, 429–438.

Kadik, A.A., Koltashev, V.V., Kryukova, E.B., Plotnichenko, V.G., Tsekhonya, T.I., Kononkova, N.N., 2015. Solubility of nitrogen, carbon, and hydrogen in $FeO–Na_2O–Al_2O_3–SiO_2$ melt and liquid iron alloy: influence of oxygen fugacity. Geochem. Int. 53, 849–868.

Kerridge, J.F., 1985. Carbon, hydrogen and nitrogen in carbonaceous chondrites: abundances and isotopic compositions in bulk samples. Geochim. Cosmochim. Acta 49, 1707–1714.

Li, Y., Dasgupta, R., Tsuno, K., 2015. The effects of sulfur, silicon, water, and oxygen fugacity on carbon solubility and partitioning in Fe-rich alloy and silicate melt systems at 3 GPa and 1600 °C: implications for core–mantle differentiation and degassing of magma oceans and reduced planetary mantles. Earth Planet. Sci. Lett. 415, 54–66.

Li, Y., Marty, B., Shchekal, S., Zimmermann, L., Keppler, H., 2016. Nitrogen isotope fractionation during terrestrial core–mantle separation. Geochem. Perspect. Lett. 2, 138–147.

Libourel, G., Marty, B., Humbert, F., 2003. Nitrogen solubility in basaltic melt. Part I. Effect of oxygen fugacity. Geochim. Cosmochim. Acta 679, 4123–4135.

Marty, B., 2012. The origins and concentrations of water, carbon, nitrogen and noble gases on Earth. Earth Planet. Sci. Lett. 313, 56–66.

McDonough, W.F., Sun, S.S., 1995. The composition of the Earth. Chem. Geol. 120, 223–253.

Médard, E., McCammon, C.A., Barr, J.A., Grove, T.L., 2008. Oxygen fugacity, temperature reproducibility, and H_2O contents of nominally anhydrous piston-cylinder experiments using graphite capsules. Am. Mineral. 93, 1838–1844.

Miyazaki, A., Hiyagon, H., Sugiura, N., Hirose, K., Takahashi, E., 2004. Solubilities of nitrogen and noble gases in silicate melts under various oxygen fugacities: implications for the origin and degassing history of nitrogen and noble gases in the Earth. Geochim. Cosmochim. Acta 68, 387–401.

Morbidelli, A., Chambers, J., Lunine, J.I., Petit, J.M., Robert, F., Valsecchi, G.B., Cyr, K.E., 2000. Source regions and timescales for the delivery of water to the Earth. Meteorit. Planet. Sci. 35, 1309–1320.

Mosenfelder, J.L., Le Voyer, M., Rossman, G.R., Guan, Y., Bell, D.R., Asimow, P.D., Eiler, J.M., 2011. Analysis of hydrogen in olivine by SIMS: evaluation of standards and protocol. Am. Mineral. 96, 1725–1741.

Mysen, B.O., Fogel, M.L., 2010. Nitrogen and hydrogen isotope compositions and solubility in silicate melts in equilibrium with reduced (N+H)-bearing fluids at high pressure and temperature: effects of melt structure. Am. Mineral. 95 (7), 987–999.

Pahlevan, K., Stevenson, D.J., 2007. Equilibration in the aftermath of the lunar-forming giant impact. Earth Planet. Sci. Lett. 262 (3), 438–449.

Paju, M., Viefhaus, H., Grabke, H.J., 1988. Phosphorus segregation in austenite in Fe–P–C, Fe–P–B and Fe–P–C–B alloys. Steel Res. 59 (8), 336–343.

Righter, K., 2003. Metal–silicate partitioning of siderophile elements and core formation in the early Earth. Annu. Rev. Earth Planet. Sci. 31 (1), 135–174.

Roskosz, M., Bouhifd, M.A., Jephcoat, A.P., Marty, B., Mysen, B.O., 2013. Nitrogen solubility in molten metal and silicate at high pressure and temperature. Geochim. Cosmochim. Acta 121, 15–28.

Rubie, D.C., Frost, D.J., Mann, U., Asahara, Y., Nimmo, F., Tsuno, K., Palme, H., 2011. Heterogeneous accretion, composition and core–mantle differentiation of the Earth. Earth Planet. Sci. Lett. 301, 31–42.

Rubie, D.C., Jacobson, S.A., Morbidelli, A., O'Brien, D.P., Young, E.D., de Vries, J., Frost, D.J., 2015. Accretion and differentiation of the terrestrial planets with implications for the compositions of early-formed Solar System bodies and accretion of water. Icarus 248, 89–108.

Sarafian, A.R., Nielsen, S.G., Marschall, H.R., McCubbin, F.M., Monteleone, B.D., 2014. Early accretion of water in the inner solar system from a carbonaceous chondrite-like source. Science 346, 623–626.

Schlichting, H.E., Sari, R.E., Yalinewich, A., 2015. Atmospheric mass loss during planet formation: the importance of planetesimal impacts. Icarus 247, 81–94.

Siebert, J., Badro, J., Antonangeli, D., Ryerson, F.J., 2013. Terrestrial accretion under oxidizing conditions. Science 339, 1194–1197.

Siwka, J., 2008. Equilibrium constants and nitrogen activity in liquid metals and iron alloys. ISIJ Int. 48 (4), 385–394.

Sleep, N.H., Zahnle, K.J., 2001. Carbon dioxide cycling and implications for climate on ancient Earth. J. Geophys. Res. 106, 1373–1399.

Stanley, B.D., Hirschmann, M.M., Withers, A.C., 2014. Solubility of C–O–H volatiles in graphite-saturated martian basalts. Geochim. Cosmochim. Acta 129, 54–76.

Tucker, J.M., Mukhopadhyay, S., 2014. Evidence for multiple magma ocean outgassing and atmospheric loss episodes from mantle noble gases. Earth Planet. Sci. Lett. 393, 254–265.

Von der Handt, A., Dalou, C., 2016. Quantitative EPMA of nitrogen in silicate glasses. Microsc. Microanal. 22 (S3), 1810–1811.

Wade, J., Wood, B.J., 2005. Core formation and the oxidation state of the Earth. Earth Planet. Sci. Lett. 236 (1), 78–95.

Wagner, C., 1962. Thermodynamics of Alloys. Addison–Wesley, Reading, MA.

Walker, R.J., 2009. Highly siderophile elements in the Earth, Moon and Mars: update and implications for planetary accretion and differentiation. Chem. Erde 69, 101–125.

Wang, Z., Becker, H., 2015. Ratios of S, Se, and Te in the silicate Earth require a volatile-rich late veneer. Nature 499, 328–331.

Wood, B.J., 1993. Carbon in the core. Earth Planet. Sci. Lett. 117 (3), 593–607.

Wood, B.J., Li, J., Shahar, A., 2013. Carbon in the core: its influence on the properties of core and mantle. Rev. Mineral. Geochem. 75, 231–250.

Xirouchakis, D., Hirschmann, M.M., Simpson, J.A., 2001. The effect of titanium on the silica content and on mineral-liquid partitioning of mantle-equilibrated melts. Geochim. Cosmochim. Acta 65, 2201–2217.

York, D., 1966. Least-squares fitting of a straight line. Can. J. Phys. 44, 1079–1086.

Zhang, H.L., Hirschmann, M.M., Cottrell, E., Newville, M., Lanzirotti, A., 2016. Structural environment of iron and accurate determination of $Fe^{3+}/\Sigma Fe$ ratios in andesitic glasses by XANES and Mössbauer spectroscopy. Chem. Geol. 428, 48–58.

Please cite this article in press as: Dalou, C., et al. Nitrogen and carbon fractionation during core–mantle differentiation at shallow depth. Earth Planet. Sci. Lett. (2016), http://dx.doi.org/10.1016/j.epsl.2016.10.026